INTERNATIONAL JOURNAL FOR NUMERICAL METHODS IN FLUIDS, VOL. 5, 43–70 (1985)

A FINITE ELEMENT FOR INCOMPRESSIBLE PLANE FLOWS OF FLUIDS WITH MEMORY

BARRY BERNSTEIN, DAVID S. MALKUS* AND ELWOOD T. OLSEN

Department of Mathematics, Illinois Institute of Technology, Chicago, IL60616, U.S.A.

SUMMARY

Flows of fluids with single-integral memory functionals are considered. Evaluation of the stress at a material point involves the deformation history of that point, and a dominant computational cost in finite element approximation is the construction of streamlines. It is shown that the simple crossed-triangle macro-element is in many ways an ideal finite element for the difficult non-linear, non-self-adjoint problem. The question as to whether this element produces convergent velocity and pressure solutions is addressed in the light of its failure to satisfy the discrete LBB condition. The effect of the element's ill-disposed ('spurious') pressure modes is discussed, and a pressure smoothing scheme is given which gives good results in Newtonian and non-Newtonian flows at various Reynolds and Deborah numbers. As an example of the element's success in modelling such flows, the problem of pressure differences in flows over transverse slots is studied numerically. The results are compared with experimental observations of such flows. The effect of fluid memory on the relation between first normal-stress differences and pressure differences is investigated.

KEY WORDS Finite Element Incompressible Flow Non-Newtonian Error Estimate Crossed Triangles

1. INTRODUCTION

The central difficulty in solving flow problems with memory dependence is that the stress at a material point depends on the deformation history of that point. If one limits oneself to consideration of stationary solutions, the problem is somewhat simplified, since only a single velocity field determines the stress. If one considers finite element approximations, there is a further simplification in that every particle's deformation history is specified by a finite number of nodal degrees of freedom, the assumed interpolations, and often an assumed far-field solution (a 'predecessor flow'). Early attempts to develop methods based on these observations were plagued by a variety of difficulties.[1,2] One of the most basic problems was the calculation of strain at historical times relative to the present configuration This involves the construction of one or more particle paths per finite element, passing through many adjacent elements in highly elastic fluids.

The purpose of this paper is to show that a particular finite element is ideal for such computations—allowing the determination of virtually exact relative strains in a finite element trial velocity field. The element is the crossed-triangle macroelement, discovered by Nagtigaal *et al.*[3] and analysed by Mercier.[4] We refer to this element as the NRC element (for 'Nagtigaal redundant constraint'). This element fails, in a most dramatic way, to satisfy the discrete LBB condition. Therefore much of the discussion in this paper centres on the deceptively simple question as to whether the element can be expected to work even in Stokes flow. We will show that

* Present address: Mathematics Research Center, University of Wisconsin–Madison, Madison, WI53705, U.S.A.

0271–2091/85/01 0043–28$02.80

Received 10 July 1983
Revised 1 March 1984

the failure of the element to satisfy the LBB condition and the reasons for its success are two sides of the same coin, and are explainable in terms of an error analysis which does not require the LBB condition.

In non-Newtonian flows, normal forces are crucially important, which implies that accurate pressures must be obtainable from elements chosen for these flows. Because the NRC element fails the LBB condition, it needs a post-processing of the computed pressures to remove unstable modes.[5] We demonstrate a simple and efficient projection method, which has worked well in computational practice. We present numerical evidence which shows that convergence of smoothed pressures occurs in Stokes flow problems with known exact solutions. We give evidence of the NRC element's success in modelling Newtonian and non-Newtonian fluids when inertial effects are included. We consider only plane flows here, but recent related work[6] shows that the axisymmetrical version of the NRC element[7] has the same attractive properties as the plane NRC element.

This paper serves as a companion to Reference 8; here the emphasis is on the necessity for and the apparent success of the NRC element in modelling steady flows of memory fluids. The numerical results are presented primarily as evidenee of the satisfactory performance of the NRC element, though we do attempt to place our results in the context of their possible rheological significance. In Reference 8, the emphasis is on the presentation of an over-all picture of the numerical method, a report of the computational performance of the method, and a more detailed investigation of the rheological implications of results similar to those reported in this paper.

2. STEADY FLOWS OF MEMORY FLUIDS

2.1. *Equations of motion*

We solve the equations of steady flow,

$$\nabla\cdot\boldsymbol{\sigma} + \mathbf{F} = \rho(\mathbf{u}\cdot\nabla)\mathbf{u} \tag{1}$$

for a velocity field, $\mathbf{u}$. Incompressibility implies $\rho =$ constant and

$$\begin{aligned} \boldsymbol{\sigma} &= \boldsymbol{\sigma}' - p\mathbf{I} \\ \nabla\cdot\mathbf{u} &= 0 \end{aligned} \tag{2}$$

for a suitably chosen hydrostatic pressure function, p.

2.2. *The constitutive equations*

The constitutive equations we employ are of the following form proposed by Curtiss and Bird:[9]

$$\begin{aligned} \boldsymbol{\sigma}'' &= \mu_0\left[T_d^{-2}\int_{-\infty}^{0}\mathbf{A}_0(\tau)m_1(\tau)\,d\tau + \varepsilon T_d^{-1}\int_{-\infty}^{0}\mathbf{B}_0(\tau)m_2(\tau)\,d\tau\right] \\ \boldsymbol{\sigma}' &= \boldsymbol{\sigma}'' - \tfrac{1}{2}(\sigma''_{11}+\sigma''_{22})\mathbf{I} \end{aligned} \tag{3}$$

T_d is the disengagement time. Its magnitude determines the effective memory of the fluid. ε is the link-tension coefficient of the Curtiss–Bird model.[9] The kinematic tensors $\mathbf{A}_0$ and $\mathbf{B}_0$ are functions of the Cauchy and Finger strain tensors[10,11] of the deformation which carries the fluid from its reference state at time $\tau = 0$ to its configuration at historical time τ. $\mathbf{B}_0$ is also a function of the strain-rate, $\dot{\gamma}(0)$, at the present time $\tau = 0$. In our computations we have employed Currie's approximation to $\mathbf{A}_0$ and $\mathbf{B}_0$.[10] The memory functions of equation (3) are given by (keeping in

mind that $\tau \leqslant 0$):

$$m_1(\tau) = \frac{96}{\pi^4} \sum_{k=0}^{\infty} \exp\left[(2k+1)^2 \frac{\tau}{T_d}\right] \tag{4}$$

$$m_2(\tau) = \frac{192}{\pi^4} \sum_{k=0}^{\infty} \frac{\exp\left[(2k+1)^2 \frac{\tau}{T_d}\right]}{(2k+1)^2}$$

With this normalization, the parameter μ_0 may be used to adjust the zero-shear viscosity,[9] which is

$$\eta(0) = \mu_0(1 + 2\varepsilon/3) \tag{5}$$

It should be noted that both $\mathbf{A}_0$ and $\mathbf{B}_0$ are functions of the position variable and are, in principle, defined everywhere in the domain of the problem. The time dependence implied by equation (3) arises by evaluating these tensors along the historical path followed by a particle which is at point $\mathbf{x}_0$ at time $\tau = 0$. Thus, both of the integrals in equation (3) are path integrals along a path parameterized by τ. Construction of the path and evaluation of the path integral are numerical procedures crucial to the success of our methods and will be discussed thoroughly below. With $\varepsilon = 0$, the Curtiss–Bird equation (3) becomes identical to the Doi–Edwards equation,[12] and is a constitutive equation of the BKZ type.[11] Many equations have a form similar to that described here[11] and can be treated by techniques described below. A simple example is the Maxwell fluid equation which can be obtained from equation (3) by setting $\varepsilon = 0$, choosing $\mathbf{A}_0$ to be the Finger-strain tensor, and taking $m_1(\tau) = e^{\tau/T_d}$. The computations of Reference 1 were carried out with this model, and the interested reader may find more background material on memory fluid problems there.

We will shortly describe the calculation of the integrand of equation (3) at various historical times, given a finite element trial velocity field. Presuming that this can be done, the evaluation of the stress can be carried out in analogy to the Laguerre integration employed in References 1 and 2. Quadrature formulae with specified degrees of precision with respect to the weighting functions $m_1(\tau)$ and $m_2(\tau)$ can be generated by classical orthogonal polynomial techniques.[13,14] The time integral in equation (3) is replaced by a finite weighted sum:

$$\int_{-\infty}^{0} f(s)m(s)\,ds \approx \sum_i \omega_i f(\tau_i) \tag{6}$$

where $f(s)$ can be either integrand of equation (3) and $m(s)$ the corresponding memory function. Then ω_i and τ_i are the weights and points computed once and for all for the appropriate memory function.

2.3. *The Galerkin equation*

As in Reference 1, we employ a standard Galerkin form of the equations of motion, in which the incompressibility is enforced by a penalty[15–17]

$$\int_{\Omega} [\boldsymbol{\sigma}' \cdot \nabla \mathbf{v} + 2z(\nabla \cdot \mathbf{u})(\nabla \cdot \mathbf{v}) + \rho[(\mathbf{u} \cdot \nabla)\mathbf{u}] \cdot \mathbf{v} - \mathbf{v} \cdot \mathbf{F}]\,d\Omega = 0 \tag{7}$$

where z is the penalty parameter and Ω is the spatial domain of the problem. Pressure is computed by

$$p = -2z\nabla \cdot \mathbf{u} \tag{8}$$

Equation (7) is restricted to $\mathbf{u}$, $\mathbf{v}$ drawn from a finite element trial space, S^h. Given any estimate $\mathbf{u}^h \in S^h$ for the solution, we need to be able to compute the residual of equation (7) on which to base an iterative correction scheme. In order to do this, a spatial numerical integration scheme must be employed, which results in a discrete finite sum in place of the space integral in equation (7). The iterative correction scheme which is currently employed is the inverse Broyden method[8,18] which iterates to a solution of equation (7) without the need for an exact tangent matrix.[1] What is needed to complete this scheme is some way to compute the integrand of equation (3) at the temporal integration points. This calculation is the dominant computational cost of our procedure. A choice of finite element suitable to employment in penalty methods which makes this computation easy in the central focus of what follows.

A non-linear iteration scheme using one or many evaluations of the tangent matrix—Newton's or modified Newton's method[18]—does seem possible and, indeed, highly desirable. The problem is that such a tangent matrix would be neither banded nor symmetric.[1,8,19] New technology is required both to compute such a tangent matrix and to solve the resulting linear systems.

3. COMPUTATION OF THE MEMORY INTEGRAND

Since the spatial integrand has become a weighted sum with the employment of a spatial integration formula, the memory portion of this approximation can be written[1]

$$\sum_e \sum_{k=1}^{m_e} \theta_k^e \boldsymbol{\sigma}'(\xi_k^e) \cdot \nabla \mathbf{v}(\xi_k^e) \tag{9}$$

where θ_k^e is a weight, ξ_k^e an integration point in element e, in which there are m_e integration points. A standard element integration scheme can be used; the other contributions to equation (7) can be computed using appropriate reduced or upwinded[20] integration rules as required. The point is that the stress at time $\tau = 0$ at particles ξ_k^e is needed. This can be accomplished if the relative strain referred to these particles can be computed.[1]

3.1. *Particle tracking*

Let $\mathbf{x}(\tau)$ be the path followed by a particle which resides at ξ_k^e at time $\tau = 0$. Let $\mathbf{F}_0(\tau)$ denote the gradient of the deformation[1] carrying ξ_k^e to $\mathbf{x}(\tau)$. These are related to a steady velocity field $\mathbf{u}^h$ by the tracking equations:[1,2,21]

$$\begin{aligned} \dot{\mathbf{x}}(\tau) &= \mathbf{u}^h[\mathbf{x}(\tau)] \\ \mathbf{x}(0) &= \xi_h^e \\ \dot{\mathbf{F}}_0(\tau) &= \nabla \mathbf{u}^h[\mathbf{x}(\tau)]\mathbf{F}_0(\tau) \\ \mathbf{F}_0(0) &= \mathbf{I} \end{aligned} \tag{10}$$

The Cauchy and Finger strain tensors are readily computed from $\mathbf{F}_0(\tau)$, and in turn $\mathbf{A}_0(\tau)$ and $\mathbf{B}_0(\tau)$. These are needed only at the temporal integration points, τ_i, of equation (6). Further details of the tracking procedure may be found in Reference 1. Suffice it to say that if equations (10) can be solved for a $\mathbf{u}^h \in S^h$—exactly or approximately—our method can proceed.

3.2. *Eliminating tracking: the stream and drift functions*

In Reference 2, a predictor–corrector method for solving the path equations of equations (10) was employed; similar methods have been proposed in finite-difference models.[22] The approach we

have attempted is to obtain elementwise analytic solutions. Suppose such a solution is known on one element, it can be extended from element to element by substituting interface conditions for the initial conditions in equations (10).[1] By construction of the particle path from one element boundary to another, the whole path can be constructed and strain accumulated.[1] But suppose further that on each finite element a stream function is known, then its level curves and their intersections with the element boundaries determine the particle path for a particle in the flow-field $\mathbf{u}^h$ and an expression for the strain at time $\tau = \tau_i$. Transit times can be determined for two points on the same streamline, $\mathbf{x}(t)$ and $\mathbf{x}(\tau)$, if a 'drift function' is known[14] for which

$$w[\mathbf{x}(t)] - w[\mathbf{x}(\tau)] = t - \tau \tag{11}$$

In view of the fact that particle paths may be pieced together from element to element, all that is required is knowledge of the drift function on each element. This can be determined in principle by finding a function $w(\mathbf{x})$ whose material derivative in the element flow is the constant 1. But, except for special, simple elements, this cannot be done analytically.

If the suppositions of the previous paragraph can be realized, the tracking procedure becomes one of piecing together element streamlines emanating from ξ_k^e, accumulating $\mathbf{F}_0(\tau)$ at element interfaces[1] and evaluating $\mathbf{F}_0(\tau_i)$ when the finite element is encountered which contains the point $\mathbf{x}(\tau_i)$. We turn our attention to a remarkable finite element, which up to an order $1/z$, has true streamlines, is suitable for employment in penalty methods, and for which both $w(\mathbf{x})$ and $\mathbf{F}_0(\tau)$ are known analytically in each element in terms of nodal values. Yet this element is a simple, geometrically flexible C_0 element.

4. THE NRC MACROELEMENT

As illustrated in Figure 1, the NRC element is a quadrilateral formed by four linear triangles[23] whose interior sides define the diagonals of the quadrilateral. A standard area–co-ordinate[23] transformation is used for generation of all element quantities from a reference triangle. The geometry of each macro is uniquely specified by specifying the corner co-ordinates, $\mathbf{S}_i^e$ (the location of the central node, $\mathbf{C}^e$, is uniquely determined by $\mathbf{S}_i^e$). If static condensation[24] is used on the central node, assembly and band/profile structure are the same for this element as for the bilinear isoparametric rectangle,[24] which implies that much code can be shared between implementations of the two elements. Note that the NRC element requires the additional computational expense of static condensation and recovery of central nodal values. This is substantial in view of the evidence presented below that the elements are equally accurate. What is gained, however, is crucial to the success of the method presented here.

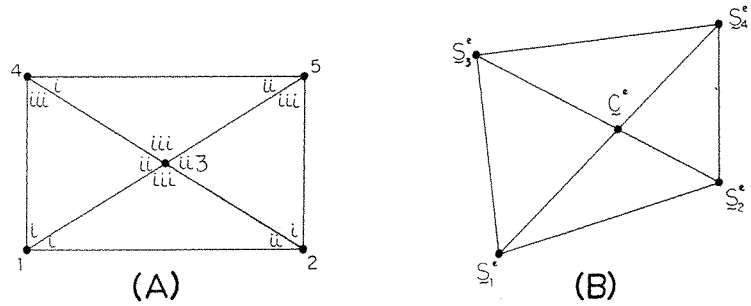

Figure 1. NRC macroelement showing (A) local element numbering and nodal numbering scheme and (B) global nodal co-ordinate vectors. Note that $\mathbf{C}_e$ lies on the intersection of macro diagonals

We employ a one-point centroidal integration formula on all terms of equation (7). Note that for Stokes flow (i.e. let $\rho = 0$ and take the limit of equation (7) as $T_d \mapsto 0$), this formula is exact. Let T^h denote the trial space of piecewise constant pressures, based on the individual triangles. Consider the following related Galerkin equations:

(A) Lagrange multiplier

$$\int_\Omega [\boldsymbol{\sigma}' \cdot \nabla \mathbf{v}^h - p^h \nabla \cdot \mathbf{v}^h - q^h \nabla \cdot \mathbf{u}^h + \rho[(\mathbf{u}^h \cdot \nabla)\mathbf{u}^h] \cdot \mathbf{v}^h - \mathbf{v}^h \cdot \mathbf{F}] d\Omega = 0, \quad \forall \mathbf{v}^h \in S^h, \quad q^h \in T^h$$

(B) Perturbed Lagrangian

$$\int_\Omega [\boldsymbol{\sigma}' \cdot \nabla \mathbf{v}^h - p^h \nabla \cdot \mathbf{v}^h - q^h \nabla \cdot \mathbf{u}^h + \rho[(\mathbf{u}^h \cdot \nabla)\mathbf{u}^h] \cdot \mathbf{v}^h - \frac{1}{2z} p^h q^h - \mathbf{v}^h \cdot \mathbf{F}] d\Omega = 0, \quad \forall \mathbf{v}^h \in S^h, \quad q^h \in T^h$$

The equivalence theorem of Reference 16, which generalizes that of Reference 15 to non-self-adjoint problems, implies that when the one-point formula is applied uniformly to (A), (B) and equation (7), equation (7) and (B) produce the same solutions. We assume that conditions are satisfied that guarantee the convergence of these solutions to the solution of (A) as $z \mapsto \infty$ (see, for example, Reference 17), though we know of no rigorous proof in the non-Newtonian case. Note that the integration is exact for Stokes flow and for the pressure terms for any T_d and ρ.

One may easily deduce that for (A)

$$\int_\Omega q^h \nabla \cdot \mathbf{u}^h d\Omega = 0, \quad \forall q^h \in T^h \tag{12}$$

and $\nabla \cdot S^h \subseteq T^h$. Thus $\nabla \cdot \mathbf{u}^h = 0$ pointwise for any solution to (A). For (B) or equation (7)

$$\int_\Omega q^h \nabla \cdot \mathbf{u}^h d\Omega = -\frac{1}{2z} \int_\Omega q^h p^h d\Omega, \quad \forall q^h \in T^h \tag{13}$$

With the NRC element, we can set $q^h = \nabla \cdot \mathbf{u}^h|_e + \frac{1}{2z} p^h|_e$ and thus deduce from equation (13) that

$$\nabla \cdot \mathbf{u}^h = -\frac{1}{2z} p^h \tag{14}$$

pointwise in element interiors. We should point out that only very special elements, such as the NRC, have discrete Lagrange multiplier solutions which satisfy $\nabla \cdot \mathbf{u}^h = 0$ and discrete penalty solutions which satisfy equation (14). It is more usual for the right-hand side of equation (14) to involve additional terms which are governed by mesh spacing and do not vanish in the infinite limit of the penalty. The bilinear/constant-p elements of Reference 1 have this feature, and the larger compressibility of the discrete solutions obtained using this element probably contributed to its less than adequate performance.[1]

We next outline tracking procedures used with the NRC element. In order to evaluate equation (3) at ξ_k^e we must, as already noted, evaluate the strains along the historical path of the particle which is at ξ_k^e at $\tau = 0$. What follows will apply rigorously to a Lagrange multiplier solution, which in view of equation (14) and the fact we take $z = O(10^6)$, is a minor perturbation. We employ iterative schemes for which the linear constraint equations (12) or (13) are satisfied at each iteration, therefore the above results apply to $\mathbf{u}^h$, which are iterates in such schemes.

Consider a typical triangle, and define

$$\begin{aligned} \mathbf{A} &= \nabla \mathbf{u}^h = [a_{ij}] \\ \Delta &= a_{11}a_{22} - a_{12}a_{21} \\ \delta &= \sqrt{(-\Delta)} \end{aligned} \tag{15}$$

Note that since $a_{11} + a_{22} = 0$, δ is real or pure imaginary, and the eigenvalues of $\mathbf{A}$ are $\pm\,\delta$. We have an element stream function:

$$\psi(x_1, x_2) = \tfrac{1}{2}[(a_{11} - a_{22})x_1x_2 + a_{12}x_2^2 - a_{21}x_1^2] + \bar{u}_1x_2 - \bar{u}_2x_1 + c \tag{16}$$

where $\bar{u}_i$ is the ith component of $\mathbf{u}^h$ at the triangle centroid and c is an arbitrary constant. The path across the element is known implicitly as a level curve of equation (16).

Since the tracking equations (10) are linear on the triangle, we have an explicit solution[1] for the strain:

$$\mathbf{F}_0(\tau) = \cosh[\delta(\tau - \tau_e)]\mathbf{F}_0(\tau_e) + \left[\frac{\sinh[\delta(\tau - \tau_e)]}{\delta}\right]\mathbf{F}_0(\tau_e)\mathbf{A} \tag{17}$$

where τ_e is the time of encounter with the boundary of the triangle, as illustrated in Figure 2. Equation (17) is used when an element is encountered which contains $\mathbf{x}(\tau_i)$.

Particle paths need not actually be generated. Only the intersections of the path across a triangle with the triangle's boundaries we needed. They are obtained by finding $\mathbf{x}_o$ on the straight line defining the triangle boundary satisfying $\psi(\mathbf{x}_o) = \psi[\mathbf{x}(\tau_e)]$. This can be done with the quadratic formula. All that is needed to determine if a time integration point, τ_i, is in the current triangle is to find the time, τ_o, of encounter with $\mathbf{x}_o$, using the drift function with $\mathbf{x}_e = \mathbf{x}(\tau_e)$,

$$w(\mathbf{x}_o) - w(\mathbf{x}_e) = \tau_o - \tau_e \tag{18}$$

The explicit drift function of linear elements was derived by one of us (Bernstein[14]). There are three cases according to the characteristics of the path equation (10) system:

Drift function

Case 1: hyperbolic, $\Delta < 0$.

$$w(\mathbf{x}) = \frac{1}{\sqrt{|\Delta|}} \ln \phi + f(\psi)$$

$$\phi = a_{21}x_1 + (\sqrt{|\Delta|} - a_{11})x_2 + \frac{a_{21}\bar{u}_1}{\sqrt{|\Delta|}} + (\sqrt{|\Delta|} - a_{11})\frac{\bar{u}_2}{\sqrt{|\Delta|}}$$

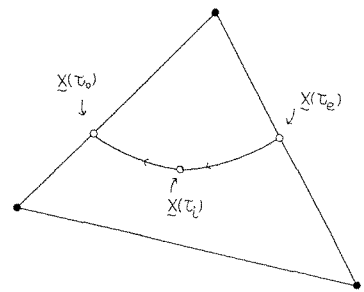

Figure 2. A conic streamline/particle path across an NRC subtriangle; $\mathbf{x}(\tau_e)$ and $\mathbf{x}(\tau_o)$ are particle positions at historical times τ_e and τ_o of boundary encounter, and $\mathbf{x}(\tau_i)$ is the position of at which a temporal integration point is encountered

Case 2: elliptic, $\Delta > 0$.

$$w(\mathbf{x}) = \frac{1}{\delta}\tan^{-1}\phi + f(\psi)$$

$$\phi = \frac{\delta x_2 + \frac{1}{\delta}(a_{11}\bar{u}_2 - a_{21}\bar{u}_1)}{a_{21}x_1 - a_{11}x_2 + \bar{u}_2}$$

Case 3: parabolic, $\Delta = 0$.

$$w(\mathbf{x}) = \phi + f(\psi)$$

For case 3 there are several separate subcases for ϕ which may be found in Reference 6. The $f(\psi)$ in each case denotes an arbitrary function of the stream function which is not needed in equation (18), since $\mathbf{x}_0$ and $\mathbf{x}_e$ are on the same level curve. Note that the element characteristics determine the conic family to which the element streamlines belong. The multiple values of the inverse tangent properly give multiple arrival times corresponding to particle circulation in a vortex. The streamlines only close in an element containing the centre of a vortex; elements may be elliptic, whether or not they contain vortex centres.

These analytic properties of the NRC element have led to a substantial improvement over the procedure described in Reference 1. There the bilinear element was employed with an assumed constant-gradient field for the purposes of tracking. This had two serious drawbacks: first, on regular meshes this is equivalent to using uniform reduced integration; secondly, equation (14) does not hold, thus there is compressibility error as a function of the mesh spacing. But the NRC fails to satisfy the discrete LBB condition.[5,17,25–28] There is then a serious question as to whether the element is stable even for Stokes flow.

5. THE ILL-DISPOSED PRESSURES OF THE NRC ELEMENT

In Reference 29 the term 'spurious mode' is applied to the pressures $c^h \in T^h$ which satisfy

$$\int_\Omega c^h \nabla \cdot \mathbf{v}^h \, d\Omega = 0, \qquad \forall \mathbf{v}^h \in S^h \tag{19}$$

and differ from a constant 'hydrostatic mode' which occurs in some problems. These c^h have also been referred to as 'chessboards'[30] or 'chequerboards' owing to their geometric pattern. We prefer to refer to these modes as 'ill-disposed' following Reference 31—without the negative connotation which has become attached to such c^h. In Reference 31 it is argued that ill-disposed modes play no role in determining natural or physical modes; likewise they may lead to inconsistent algebraic systems. But, alternatively, each ill-disposed mode has a dual velocity mode which is weakly incompressible. A prime example of this simple algebraic consequence of ill-disposed pressures is provided by the NRC element.

A simple count of unconstrained degrees of freedom[15] for the NRC element according to

$$N_{\text{udof}} = \dim S^h - \dim T^h \tag{20}$$

on sequences of regular meshes leads to the conclusion that the NRC is grossly overconstrained—as are other arrangements of linear triangles.[4,15] Let $U^h \subseteq T^h$ be the subspace satisfying equation (19) of ill-disposed modes and possibly the hydrostatic mode. What the algebraic argument of

Reference 31 is saying is that a careful constraint count gives

$$N_{\text{udof}} = \dim S^h - \dim T^h + \dim U^h \tag{21}$$

Mercier[4] recognized that dim U^h was significant for the NRC. Given $\mathbf{v}^h \in S^h$, consider a typical NRC macro in any mesh, and let e_1, e_2, e_3, e_4 denote the four subtriangles, ordered as in Figure 1. Mercier proved that

$$\nabla\cdot\mathbf{v}^h|e_1 - \nabla\cdot\mathbf{v}^h|e_2 - \nabla\cdot\mathbf{v}^h|e_3 + \nabla\cdot\mathbf{v}^h|e_4 = 0. \tag{22}$$

Mercier then argues that for T^h as we have chosen, only three of the four incompressibility constraints are independent, since setting $\nabla\cdot\mathbf{v}^h = 0$ on three triangles forces it to be zero on the fourth.

This argument which shows that the NRC is not overconstrained can be turned around to show that the NRC also has many ill-disposed modes. Consider again our typical macro, labelled M, and define

$$c_M^h \equiv \begin{cases} \pm 1/a^{e_i}, & \text{on triangle } e_i[+, i = 1,4 \text{ and } -, i = 2,3] \\ 0, & \text{outside of macro } M \end{cases} \tag{23}$$

where a^{e_i} is the area of triangle e_i. Now

$$\int_\Omega c_M^h \nabla\cdot\mathbf{v}^h \mathrm{d}\Omega = \int_M c_M^h \nabla\cdot\mathbf{v}^h \mathrm{d}\Omega = \sum_{i=1}^{4} a^{e_i}[c_M^h \nabla\cdot\mathbf{v}^h]_{e_i} \tag{24}$$

since c_M^h and $\nabla\cdot\mathbf{v}^h$ are constant on triangles. But substituting equations (22) and (23) into equation (24) shows that c_M^h satisfies equation (19), thus $c_M^h \in U^h$. Note that there is one such ill-disposed mode for each macro. It is not hard to show that on regular rectangular meshes with boundary conditions which cause the bilinear/constant-p element[29] to have a chequerboard mode, the NRC has a similar chequerboard mode satisfying equation (19), constant on each macro and alternating in sign between macros.[32] We refer to this as the 'global ill-disposed mode' and those of equation (23) as 'local ill-disposed modes' for obvious reasons.

What we have seen is an instance of a simple algebraic truth[31]—redundant constraints and ill-disposed modes are one and the same. The NRC has a favourable constraint count only because it has 'spurious pressure modes'. The global mode of the NRC can cause algebraic consistency problems related to inhomogeneous boundary conditions.[5,29] This must be avoided the way it is with bilinear/constant-p rectangles. We shall now prove that the local ill-disposed modes cannot lead to inconsistency.

Inhomogeneous boundary conditions are often imposed as described in Reference 20. S^h is taken to be the trial space satisfying homogeneous boundary conditions wherever essential b.c. are specified. u_0^h is chosen to be zero at all mesh nodes except those which coincide with boundaries on which inhomogeneous essential b.c. are specified. At those nodes $\mathbf{u}_0^h$ interpolates to the inhomogeneous data. Thus $\mathbf{u}^h = \mathbf{w}^h + \mathbf{u}_0^h$ is sought with $\mathbf{w}^h \in S^h$ determined by the Galerkin equation. Constraint equation (12) becomes

$$\int_\Omega q^h \nabla\cdot\mathbf{w}^h \mathrm{d}\Omega = -\int_\Omega q^h \nabla\cdot\mathbf{u}_0^h \mathrm{d}\Omega \tag{25}$$

Note that equations (12) and (25) have the following algebraic solvability condition.[29,31] There is a solution $\mathbf{w}^h \in S^h$ to equations (12) and (25) only if

$$\int_\Omega c^h \nabla\cdot\mathbf{u}_0^h \mathrm{d}\Omega = 0, \quad \forall c^h \in U^h \tag{26}$$

We have

Theorem 1

Let c_M^h be a local ill-disposed mode of the NRC element, i.e. c_M^h is as in equation (23). Then for $\mathbf{u}_0^h$ as defined above, the solvability equation (26) is satisfied.

Proof. We note that the only reason equation (26) does not follow from equation (19) is that $\mathbf{u}_0^h \notin S^h$. Consider the larger space $\bar{S}^h \supseteq S^h$ of functions free on all boundaries: $\mathbf{u}_0^h \in \bar{S}^h$. Now observe that the argument of equation (24) applies equally well to all $\mathbf{v}^h \in \bar{S}^h$, since it involves only one macroelement and does not depend on the boundary conditions. QED

Remark 1.1. The above argument does not apply to the global ill-disposed mode. As with the bilinear/constant-p rectangle, the global mode occurs on some meshes because there is a c^h which is orthogonal to $\nabla \cdot S^h$ but not $\nabla \cdot \bar{S}^h$.

Remark 1.2. The local ill-disposed modes of the NRC are pieced together from ill-disposed modes of the element weak-gradient matrix[31] and are not related to boundary conditions.

Theorem 1 says that inhomogeneous boundary conditions cause no more difficulty for the NRC element than with the bilinear/constant-p element. Boundary conditions chosen so that $\mathbf{u}_0^h$ is such that equation (26) is satisfied for the global ill-disposed mode will avoid the pathologies described in Reference 29. This, however, is a long way from guaranteeing convergence of the NRC approximation, even in Stokes flow. We now turn our attention to that question.

6. APPROXIMATION ERRORS USING THE NRC IN STOKES FLOW

The ill-disposed pressures lead to a non-uniqueness of the pressure solution from the Lagrange multiplier method (A) for Stokes flow. This assumes that any algebraic inconsistency with the global mode has been avoided and results from the fact that if p_0^h is a solution, so is $p_0^h + c^h$ for $c^h \in U^h$. The velocity solution is unique.[29] The penalty method gives a unique pressure solution which tends to a representative pressure solution of the Lagrange multiplier method[28] as $z \mapsto \infty$. The question of convergence as the mesh is refined can be resolved by resolving the question for the Lagrange multiplier solutions $(\mathbf{u}^h, p_w^h)$, where

$$\int_\Omega c^h p_w^h \, d\Omega = 0, \quad \forall c^h \in U^h \tag{27}$$

which is unique.

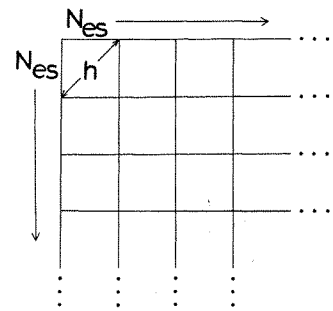

Figure 3. A regular, square, $N_{es} \times N_{es}$ mesh of NRC macroelements of diameter h

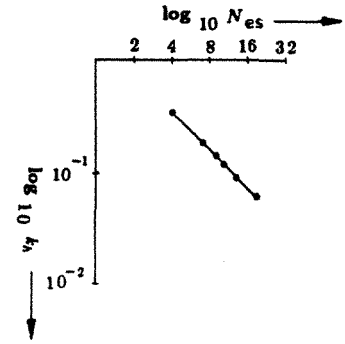

Figure 4. The 'constant' k_h with $N_{es} = 4$, 8, 10, 12, 16 and 24. log × log slope confirms that $k_h \approx Ch$

To determine whether $(\mathbf{u}^h, p_w^h)$ converges to the exact solution $(\mathbf{u}^*, p^*)$ as the mesh is refined, we first consider a generalized LBB condition:[5,28,30,31]

For q^h orthogonal to U^h in $L_2(\Omega)$:

$$\sup_{\mathbf{w}^h \in S^h, \mathbf{w}^h \neq 0} \int_\Omega \frac{q^h \nabla \cdot \mathbf{w}^h}{\| \mathbf{w}^h \|_1} d\Omega \geqslant k_h \| q^h \|_0 \tag{28}$$

where $\| \cdot \|_1$ denotes the energy norm[31] (we assume essential boundary conditions imply that the energy-norm is equivalent to the $W^{1,2}(\Omega) \times W^{1,2}(\Omega)$-norm). $\| \cdot \|_0$ denotes the $L_2(\Omega)$-norm. The desired result for $(\mathbf{u}^h, p_w^h)$ could be established if k_h were bounded away from zero independent of h; unfortunately for many NRC meshes, it is not.

Consider the meshes of Figure 3, in which one NRC is fit into each of the N_{es}^2 squares. As shown in Figure 4, a direct computation[31] on a sequence of such meshes shows that

$$k_h = \inf_{q^h \neq 0} \sup_{\mathbf{w}^h \neq 0} \int_\Omega \frac{q^h \nabla \cdot \mathbf{w}^h}{\| q^h \|_0 \| \mathbf{w}^h \|_1} d\Omega \qquad q^h \in T^h, q^h \perp U^h \text{ and } \mathbf{w}^h \in S^h \tag{29}$$

tends to zero as $O(h)$; k_h as given in equation (29) is the best possible k_h for equation (28). These numerical results have been recently confirmed by a proof that $k_h = O(h)$ on sequences of meshes of NRC elements pictured in Figure 3.[32] The numerical procedure used in the calculation of Figure 4 is, nevertheless, of great value, since it allows determination of k_h on irregular meshes which defy analytic treatment.[5] Thus it is not possible to make a general Brezzi-style estimate for $(\mathbf{u}^h - \mathbf{u}^*, p_w^h - p^*)$.

6.1. *Velocity estimates without the discrete LBB condition*

It will be convenient in what follows to use the energy inner product:[5,31]

$$a(\mathbf{u}, \mathbf{v}) = \int_\Omega \dot{\mathbf{e}} \cdot \dot{\mathbf{f}} d\Omega \tag{30}$$

where $\dot{e}_{ij} = \frac{1}{2}(u_{i,j} + u_{j,i})$ and $\dot{f}_{ij} = \frac{1}{2}(v_{i,j} + v_{j,i})$ for $i, j = 1, 2$. Thus $\| \cdot \|_1 = a(\cdot, \cdot)^{1/2}$. We consider the subspace $W^h \subseteq S^h$ of trial functions satisfying the incompressibility constraint equation (12) and define the operator

$$Z_h : H_1 \mapsto W^h \tag{31}$$

which is the projection from the space H_1 onto W^h with respect to the energy norm. H_1 is a

subspace of $W^{1,2}(\Omega) \times W^{1,2}(\Omega)$ satisfying homogeneous essential boundary conditions on some or all of the boundary of Ω. For admissible pressures in the Lagrange multiplier method we take $H_0 = L_2(\boldsymbol{\Omega})$. The exact solution $(\mathbf{u}^*, p^*)$ satisfies the continuous analogue to (A) above:

$$\begin{aligned} &a(\mathbf{u}^*, \mathbf{v}) - (p^*, \nabla\cdot\mathbf{v})_0 - (q, \nabla\cdot\mathbf{u}^*)_0 = (\mathbf{v}\cdot\mathbf{F}, 1)_0 \\ &\forall \mathbf{v}\in H_1 \text{ and } q\in H_0 \end{aligned} \tag{32}$$

where $(\cdot,\cdot)_0$ denotes the $L_2(\Omega)$ inner product. We assume that the domain, boundary conditions and $\mathbf{F}\in L_2(\Omega) \times L_2(\Omega)$ are such that $\mathbf{u}^*\in W^{k,2}(\Omega) \times W^{k,2}(\Omega)$ for $k \geqslant 2$ with $\mathbf{u}^*$ unique, and $p^*\in W^{m,2}(\Omega)$ for $m \geqslant 1$.[33] p^* may not be unique when there is a hydrostatic mode,[29] but hereafter we assume that in such cases p^* is the unique representative pressure solution for which $(p^*, 1)_0 = 0$. We now prove

Theorem 2

If $(\mathbf{u}^*, p^*)$ is the solution to equation (32) and $(\mathbf{u}^h, p_w^h)$ is the finite element solution to the Lagrange multiplier method (A) in the Stokes flow case,

$$\| \mathbf{u}^h - Z_h\mathbf{u}^* \|_1 \leqslant c \inf_{q_h\in T_h} \| q^h - p^* \|_0 \tag{33}$$

where $\|\cdot\|_1$ is the norm induced by $a(\cdot,\cdot)$ and c is a constant independent of h.

Proof. Let $q^h = 0$ in problem (A) and $q = 0$ in equation (32). Also in equation (32) let $\mathbf{v} = \mathbf{v}^h\in S^h$,

$$a(\mathbf{u}^*, \mathbf{v}^h) - (p^*, \nabla\cdot\mathbf{v}^h)_0 = (\mathbf{v}^h\cdot\mathbf{F}, 1)_0$$
$$a(\mathbf{u}^h, \mathbf{v}^h) - (p^h, \nabla\cdot\mathbf{v}^h)_0 = (\mathbf{v}^h\cdot\mathbf{F}, 1)_0$$

Subtracting gives

$$a(\mathbf{u}^h - \mathbf{u}^*, v^h) = (p^h - p^*, \nabla\cdot\mathbf{v}^h)_0$$

Now observe that $\mathbf{u}^h\in W^h$ so that $Z^h\mathbf{u}^h = \mathbf{u}^h$, thus, letting $\mathbf{v}^h = \mathbf{u}^h - Z_h\mathbf{u}^*$ and using the fact that $Z_h^2 = Z_h$ and that Z_h is self-adjoint in $a(\cdot,\cdot)$, implies

$$a(\mathbf{u}^h - \mathbf{u}^*, \mathbf{u}^h - Z_h\mathbf{u}^*) = a(\mathbf{u}^h - Z_h\mathbf{u}^*, \mathbf{u}^h - Z_h\mathbf{u}^*) = (p^h - p^*, \nabla\cdot[\mathbf{u}^h - Z_h\mathbf{u}^*])_0 \tag{34}$$

We note that the right-hand side of equation (34) may not be zero since $p^* - p^h \notin T^h$, but it is small since we can let $\bar{p}^h =$ best $L_2(\Omega)$ approximation to p^* and add zero to the right-hand side of equation (34) in the form of $(\bar{p}^h, \nabla\cdot[\mathbf{u}^h - Z_h\mathbf{u}^*])_0$. Also $(p^h, \nabla\cdot[\mathbf{u}^h - Z_h\mathbf{u}^*])_0 = 0$, which gives

$$a(\mathbf{u}^h - Z_h\mathbf{u}^*, \mathbf{u}^h - Z_h\mathbf{u}^*) = (\bar{p}^h - p^*, \nabla\cdot[\mathbf{u}^h - Z_h\mathbf{u}^*])_0 \leqslant c \| p^* - \bar{p}^h \|_0 \| \mathbf{u}^h - Z_h\mathbf{u}^* \|_1$$

The inequality follows from the boundedness of the weak divergence, whose operator norm gives c.[33] Division by $\| \mathbf{u}^h - Z_h\mathbf{u}^* \|_1$ gives the desired result. QED

Remark 2.1. This result should be compared to the classical result for unconstrained problems, which shows that the finite element solution is the best energy approximation to the exact solution. Here the f.e.m. solution is as close to the best weakly imcompressible approximation to the exact solution as the pressures are accurate.

Remark 2.2. Theorem 2 shows that the primary role of the Lagrange multiplier is to constrain the f.e.m. solution to be close to $Z_h\mathbf{u}^*$.

Remark 2.3. Only accuracy of the Lagrange multiplier space T^h is required, not the stability of the pressure approximation.

Theorem 2 is quite easily turned into an estimate for $\|\mathbf{u}^h - \mathbf{u}^*\|_1$ which does not require the LBB condition:

Theorem 3

$$\|\mathbf{u}^h - \mathbf{u}^*\|_1 \leqslant \|\mathbf{u}^* - Z_h\mathbf{u}^*\|_1 + c \inf_{q^h \in T^h} \|p^* - q^h\|_0$$

Proof. Add and subtract $\mathbf{u}^*$ and use the triangle inequality in Theorem 2. QED

Remark 3.1. The idea of constraint counting[15] was designed to give a heuristic idea of whether $\|\mathbf{u}^* - Z_h\mathbf{u}^*\|_1$ could be expected to be small based on an estimate of $N_{\text{udof}} = \dim W^h$.

Results similar to Theorem 3 have been established by others. We point out particularly the work of Mercier in Reference 34. He proves a result which differs from ours in the present application only in that he uses the standard norm on $W^{1,2}(\Omega) \times W^{1,2}(\Omega)$ rather than the energy norm. This gives different absolute constants in the estimate. Mercier also points out an interesting sharpening of our estimate which applies to the NRC element:

Corollary 3.1 (Mercier)

If the functions in W^h are weakly incompressible with respect to multipliers in H_0, then

$$\|\mathbf{u}^h - \mathbf{u}^*\|_1 = \|\mathbf{u}^* - Z_h\mathbf{u}^*\|_1$$

Proof. The right-hand side of equation (32) *is* zero in this case, implying that the right-hand side in Theorem 2 is zero. QED

Remark 3.2. The result applies to the NRC since weak incompressibility implies pointwise incompressibility which in turn implies incompressibility w.r.t. H_0 multipliers.

The work of Mercier predates ours but seems to have received less attention than it deserves because emphasis has since been placed on ensuring the optimality of $\|\mathbf{u}^* - Z_h\mathbf{u}^*\|_1$ by choice of elements which satisfy the LBB condition. Satisfaction of the LBB condition guarantees that $\|\mathbf{u}^* - Z_h\mathbf{u}^*\|_1$ is on the order of optimal approximation of strain-rates by S^h. This follows directly from the work of Brezzi.[25] There are several ways which $\|\mathbf{u}^* - Z_h\mathbf{u}^*\|_1$ can be shown to be small when the LBB condition is not satisfied. The interested reader is referred to Reference 5. We focus here on another idea of Mercier.[34]

In Reference 34 a construction is sketched which is intended to show that there is a $\mathbf{w}^h \in W^h$ with

$$\|\mathbf{w}^h - \mathbf{u}^*\|_1 \leqslant Ch\|\mathbf{u}^*\|_2$$

on rectangular domain discretized by square elements. Since the transformation of one rectangular domain to another is infinitely differentiable, a simple change of variable would lead to the same conclusion for a rectangular domain with rectangular elements. The construction in Reference 34 is very brief and contains a confusing misprint, and most important does not show how the construction can be carried out near no-slip boundaries. Consider any macroelement; the central node (node 3 in Figure 1(A)) is completely specified by the requirement that $\nabla \cdot \mathbf{w}^h = 0$. In fact for a rectangular element, it is easy to deduce that if $\mathbf{w}^h = [u^h, v^h]^T$,

$$\begin{aligned} u_3 &= \tfrac{1}{2}(u_1 + u_4 + v_1 - v_4) = \tfrac{1}{2}(u_2 + u_5 - v_2 + v_5) \\ v_3 &= \tfrac{1}{2}(u_1 - u_2 + v_1 + v_2) = \tfrac{1}{2}(-u_4 + u_5 + v_4 + v_5) \end{aligned} \tag{35}$$

where $[u_i, v_i]^T$ is the ith nodal value of $\mathbf{w}^h$ in the numbering of Figure 1. Thus if two adjacent nodes have zero velocity, the flow at node 3 must be parallel to the still boundary. If three nodes have zero velocity, the central node must also have zero velocity. It is not hard to see that Mercier's construction as given in Reference 34 does not satisfy these constraints, nor does it appear to us that there is a simple way to modify the construction appropriately so that it does.

The constraints implied by equations (35) are physically reasonable. The implication is that the triangles with two nodes on a no-slip wall must be in simple shear to satisfy the continuity equation. If one of the nodes in such a triangle is at a corner, and thus on two walls, the shear-flow must actually be still. The central nodes of wall elements are thus in a shearing boundary-layer and have correspondingly simple flows. This points out an important fact about the NRC element: equations (35) show that the central node is not really a degree of freedom in incompressible flows, rather it provides unknowns which are 'used up' in satisfying the continuity equation.

Mercier's construction appears to be correct if no b.c. are imposed. It can be modified to make $\mathbf{w}^h$ incompressible quite easily, but this seems to require the sacrifice of approximation accuracy. The best analytical result we have is that if $\mathbf{u}^*$ has three square integrable derivatives then on simple meshes of the type considered here, $\|\mathbf{w}^h - \mathbf{u}^*\|_1 \leqslant Ch\|\mathbf{u}^*\|_3$.[32] The extra smoothness required of $\mathbf{u}^*$ seems to be needed only for the proof technique, however, and numerical experiments suggest that the result of Reference 34 holds even with no-slip b.c., only requiring $\mathbf{u}^* \in W^{2,2}(\Omega) \times W^{2,2}(\Omega)$.

6.2. *Pressure estimates without the discrete LBB condition*

Let us assume that velocity estimates along the lines of the previous subsection have been obtained. Subtracting discrete and continuous weak equations as in the proof of Theorem 2 gives for all $\mathbf{v}^h \in S^h$

$$a(\mathbf{u}^h - \mathbf{u}^*, \mathbf{v}^h) = (p_w^h - p^*, \nabla\cdot\mathbf{v}^h)_0 = (p_w^h - \bar{p}^h + \bar{p}^h - p^*, \nabla\cdot\mathbf{v}^h)_0$$

where, as before, $\bar{p}^h$ is the best $L_2(\Omega)$ approximation to p^* from T^h. Thus

$$(\bar{p}^h - p_w^h, \nabla\cdot\mathbf{v}^h)_0 = (\bar{p}^h - p^*, \nabla\cdot\mathbf{v}^h)_0 - a(\mathbf{u}^h - \mathbf{u}^*, \mathbf{v}^h) \tag{36}$$

Under usual assumptions of approximation accuracy, it suffices to show that $\|p_w^h - \bar{p}^h\|_0$ is small. This does not immediately follow from equation (36) even though the right-hand side is small when $\|\mathbf{v}^h\|_1 = 1$. (The right-hand side is indeed small because $\|\mathbf{u}^h - \mathbf{u}^*\|_1$ and $\|\bar{p}^h - p^*\|_0$ are small.) The problem is twofold: first, $p_w^h - \bar{p}^h$ may have a component in U^h. The smallness of the right-hand side might then only show that this component is substantial, not that $\|p_w^h - \bar{p}^h\|_0$ is small. In Reference 5 this problem is addressed. There it is shown that with some reasonable assumptions there is an approximation $\bar{p}^h \in [\![U^h]\!]^\perp \cap T^h$ such that $\|p^* - \bar{p}^h\|_0$ is as small as the maximum of $\|\mathbf{u}_I^h - \mathbf{u}^*\|_1$ and $\|\bar{p}^h - p^*\|_0$, where $\mathbf{u}_I^h$ is the nodal interpolate to $\mathbf{u}^*$. Thus proving that $\|p^h - \bar{p}^h\|_0$ is small will suffice to produce a pressure estimate. Furthermore, since $(\bar{p}^h - \bar{\bar{p}}^h, \nabla\cdot\mathbf{v}^h)_0 = 0$ for all $\mathbf{v}^h \in S^h$, $\bar{\bar{p}}^h$ can be substituted for $\bar{p}^h$ in equation (36).

Secondly, since the constant k_h of equation (29) can evidently only be bounded by $k_h \geqslant C_1 h$ on many meshes, the best that follows from equation (36) by taking the supremum of both sides with $\|\mathbf{v}^h\|_1 = 1$ is

$$\|p_w^h - \bar{p}^h\|_0 \leqslant \frac{1}{C_1 h}[C_2\|\mathbf{u}^h - \mathbf{u}^*\|_1 + C_3\|\bar{p}^h - p^*\|_0] \tag{37}$$

$\|\bar{p}^h - p^*\|_0$ is usually $\leqslant Ch\|p^*\|_1$. We believe that $\|\mathbf{u}^h - \mathbf{u}^*\|_1 \leqslant Ch\|\mathbf{u}^*\|_2$ as discussed earlier. The best that equation (37) gives then is that $\|p_w^h - \bar{p}^h\|_0$ is bounded.

In Reference 5, it is shown that if one is willing to accept the 'dual norm'

$$\| p_w^h - \bar{p}^h \|_{-1} = \sup_{\|q\|_1 = 1} \int_\Omega q(p_w^h - \bar{p}^h) \, d\Omega$$

an estimate can be obtained for $\| p_w^h - \bar{p}^h \|_{-1}$ whose dominant term is no worse than $Ch \| p_w^h - \bar{p}^h \|_0$, which is then $O(h)$. This estimate may not be of practical value, but it does suggest that p_w^h is not meaningless, and indeed does contain valuable information. The rationale for recovering smoothed approximations to p_w^h which converge at an optimal rate will be discussed below. It is interesting to note that in a class of test problems described in Reference 5, optimal convergence rates are observed for $\| p_w^h - p^* \|_0$. A typical example employing the NRC element is pictured in Figure 5. The problem is of the form

$$\begin{aligned} \nabla^2 \mathbf{u} - \nabla p &= \mathbf{F} \quad \text{on } (0,2) \times (0,2) = \Omega \\ \mathbf{u} &= 0 \quad \text{on boundary } [(0,2) \times (0,2)] = \Gamma \end{aligned} \tag{38}$$

$\mathbf{F}$ is chosen so that the exact $\mathbf{u}^*$ and p^* are in $W^{2,2}(\Omega) \times W^{2,2}(\Omega)$ and $W^{1,2}(\Omega)$, respectively, but not in $W^{3,2}(\Omega) \times W^{3,2}(\Omega)$ and $W^{2,2}(\Omega)$. The domain is discretized with square NRC elements, and thus we have meshes of the type used in Figure 4. Thus k_h is surely tending to zero at a rate which would, by our above analysis, imply that $\| p_w^h - p^* \|_0$ is only bounded. On the other hand, curve (a) of Figure 5 shows that $\| p_w^h - p^* \|_0$ tends to zero at $O(h)$†, and according to equation (36), it does suggest that $\| \mathbf{u}^h - \mathbf{u}^* \|_1 \leqslant Ch \| \mathbf{u}^* \|_2$ also.

As is discussed in Reference 5, examples can be constructed in which $\| p_w^h - p^* \|_0$ appears to be either non-convergent or affected by oscillatory pressures. But all such cases of which we are aware seem to have singularities in the strain-rates of the exact solution (and probably the pressure). In such cases, an *ad hoc* analysis of the singularity is required to get precise estimates, but the frequency of appearance of such singularities in problems of physical importance argues that some post-processing of the 'raw' pressure, p_w^h, is always wise. This even if it does eventually prove that $\| p_w^h - p^* \|_0$ is convergent in problems where standard smoothness assumptions hold.[5] For now, at

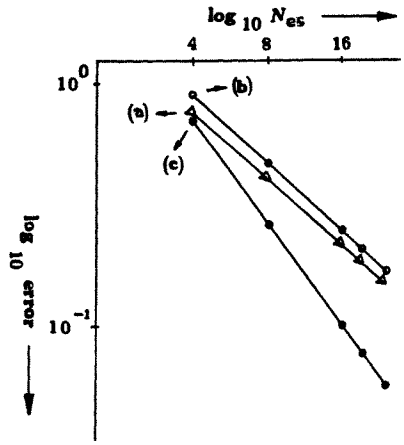

Figure 5. Convergence rate achieved by raw penalty pressures (a), macro-averaged (b), and (c) projected onto the conforming bilinears. NRC elements with $N_{es} = 4$, 8, 16, 20 and 24. Stokes problem with minimally smooth $(\mathbf{u}^*, p^*)$

† Actually, we use a penalty approximation to p_w^h, but since $z = O(10^6)$, and the errors in question are orders of magnitude larger than $1/z$, there is no doubt that this conclusion applies to p_w^h itself.

least, the post-processing to which we turn our attention is required to get estimates even for these smoother problems.

6.2.1. *Pressure smoothing.* A rationale for the post-processing of the pressures can be presented which applies the ideas of Reference 27 to the methods of Reference 20. The latter were designed to smooth oscillatory pressures which sometimes appear in f.e.m. solutions to the Navier–Stokes equations. The idea is to find an auxiliary pressure trial space, V^h, such that $L_2(\Omega)$ projection from T^h to V^h smooths out the spurious oscillations in p_w^h. Since such projection must also nullify all of U^h which is orthogonal to constants, it therefore suffices to smooth any pressure solution, p^h, to the Lagrange multiplier method (A), not necessarily p_w^h. The rationale is that if V^h is chosen to be able to approximate p^* well, and if T^h and V^h satisfy a 'posterior LBB condition' with respect to a seminorm defined using the orthoprojection

$$r_h: L_2(\Omega) \to V^h$$

then an estimate for $\tilde{p}^h = r_h p^h$ can be obtained in the $L_2(\Omega)$-norm.[5]

The posterior LBB condition is hard to prove. In Reference 27 a proof for bilinear/constant-p rectangles with V^h constructed on macro-elements is given. In Reference 32, this result is generalized to the NRC element, but the choice of V^h is computationally inconvenient. Unfortunately we know of no rigorous proof of the posterior LBB condition for the choice of V^h given below. In fact, experience seems to suggest that the scheme does not completely nullify non-constant members of U^h, and thus it cannot satisfy the posterior LBB condition. The posterior LBB condition does show us that there are at least some smoothing schemes which are rigorously guaranteed to work, if inconvenient. We rely on computational experience to give us confidence with other schemes.

From a practical standpoint, pressure smoothing of the projection variety is easy to implement: the nodal-values of $\tilde{p}^h$ are given by

$$M^{-1}\left[\int_\Omega p^h \phi_i \, d\Omega\right] \tag{39}$$

where M is the 'mass matrix' of V^h and $[\![\phi_i]\!]$ the nodal basis of V^h. If M is 'lumped',[35] then the computation involved in equation (39) is no more costly than computation of a load vector. For the NRC element we make the same choice for V^h as chosen in Reference 20 for bilinear/constant-p elements: we use the conforming bilinear elements based on the corner nodes of each macro. This produces a continuous pressure field referred to velocity nodes. We use the centroidal one-point formula in each triangle to evaluate the contribution from each macro to equation (39).

In Reference 20, it is pointed out that there may be modifications which will improve $\tilde{p}^h$ at boundary nodes. This is particularly needed at unshared corner nodes when p^h is 'chequer-boarded'. (This is the experience which suggests that this choice of V^h does not lead to satisfaction of the posterior LBB condition.) Trouble with unshared nodes is nevertheless consistent with convergence of the projected pressures, because even though V^h is a conforming space, convergence is only in $L_2(\Omega)$, and the pointwise values at nodes need not converge. We have not implemented any modification procedure, but rather prefer to apply a cautious interpretation to our results at boundary nodes. In Reference 20, it is argued that the value of unmodified $\tilde{p}^h$ at non-corner boundary nodes, shared between two elements on a straight boundary, is actually a better approximation to p^* half an element width into the flow than at the boundary. This analysis applies to projection of piecewise constant pressures onto the bilinears, but since we find that in each macro the pressure varies little from triangle to triangle, the result evidently applies to the NRC in such cases as well. We compute average values of $\dot{e}_{ij}$ and σ'_{ij} in each macro, and for the boundary-

layer elements nearest walls, associated the values of $\tilde{p}^h$ with these average quantities. We disregard the value of $\tilde{p}^h$ at domain corner nodes entirely.

In Figure 5 we illustrate the effect of applying the pressure smoothing scheme to the test problem of equation (38). Since the raw pressure p_w^h converges at an optimal rate without projection, this does not provide a good test of the smoothing. But curve (c) of Figure 5 does illustrate an interesting—and unexplained—phenomenon. The convergence rate of the smoothed pressures is $O(h^{3/2})$ as opposed to the $O(h)$ observed in p_w^h. In this test problem, we can see with certainty that the convergence rate has not been slowed down by our projection method. To provide a more critical test, we must turn our attention to problems in which the exact solution is not known.

7. NUMERICAL SOLUTION OF THE HOLE-PRESSURE THEOREM

The hole-pressure problem in the plane-flow case seems to be an ideal testing ground for the techniques presented here. The problem involves flow over a transverse slot, beginning and ending in plane Poiseuille flow as a far-field solution. As is illustrated in Figure 6, the flow is assumed to start from and return to channel flow at finite distances up- and down-stream of the slot. In the non-Newtonian case, the particle histories are known analytically outside the prescribed domain.[1] This problem has been treated numerically by several authors;[8,36–38] there are analytical predictions[8,39] and experimental observations about aspects of such flows,[38] and, finally, for low Reynolds number Newtonian flows, degree of smoothness of the exact solution can be predicted with some precision.[40]

7.1. *Pressure differences over a slot*

The difference between the total thrust on the wall at the top and bottom of a slot such as pictured in Figure 6 varies as a function of material properties of the fluid and Reynolds number.

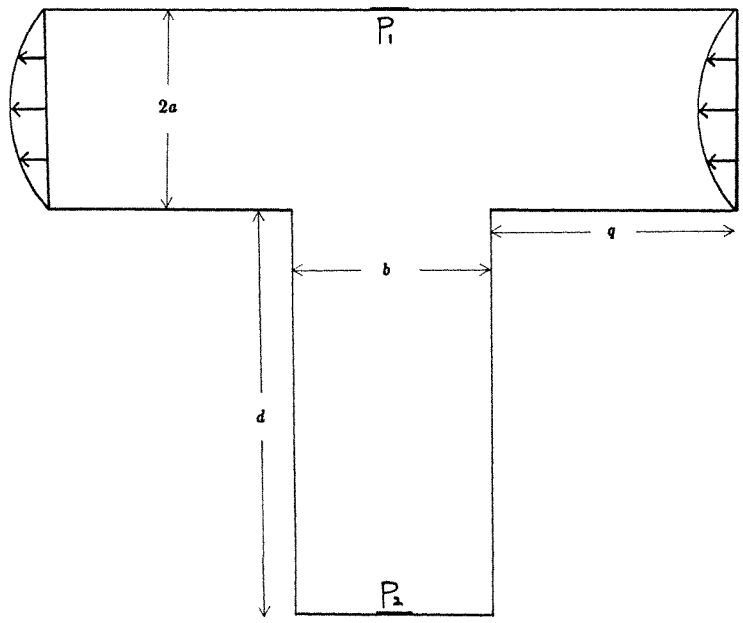

Figure 6. The cross-section of a plane channel with a deep transverse slot. P_1 and P_2 mark the locations of pressure transducers. Undisturbed channel-flow is imposed at inflow and outflow

Here we consider shear-rate/hole-based Reynolds number,[41] $R_L(s)$, and the more usual average velocity/channel width-based Reynolds number, Re:

$$Re = \frac{\rho 2aU}{\eta(0)}$$

$$R_L(\dot{s}) = \frac{\rho 2ab\dot{s}}{4\eta(\dot{s})} \tag{40}$$

where ρ is the mass-density, $2a$ the channel width, U the average velocity in undisturbed flow, $\eta(\dot{s})$ the viscosity as a function of $\dot{s}$, the wall shear-rate in undisturbed flow, and b the width of the slot. In Newtonian flow $\eta(\dot{s}) = \eta(0)$ and

$$Re/R_L = \frac{4}{3}\frac{a}{b} \tag{41}$$

but in non-Newtonian flows R_L can be dramatically larger than Re because of shear-thinning.

We define the pressure difference, P^*, as the difference between the normal stresses acting on the wall, at the indicated locations in Figure 6.

$$P^* = P_1 - P_2 \tag{42}$$

where $|P_i| = |\sigma'_{nn} - p|$, and n is the normal direction to the wall. The sign of P_i is chosen to be positive if the resulting force acts away from the interior of Ω. If we take Cartesian co-ordinate axes aligned so that the x_1-direction is the direction of undisturbed flow and the x_2-direction is the orthogonal axis in the plane of the flow, the wall shear-stress, σ, and first normal stress difference, N_1, are defined using the following stresses at the wall:

$$\sigma \equiv \sigma_{12} \tag{43}$$

$$N_1 \equiv \sigma_{11} - \sigma_{22}$$

In undisturbed channel flow of a Newtonian fluid $N_1 \equiv 0$, and in Stokes flow over a slot $P^* = 0$. Our purpose is to investigate the dependencies between $N_1, \dot{s}, \sigma, R_L(\dot{s})$ and P^*. In more detail, we focus on two hypothesis:

I. For Newtonian fluids at low $R_L(\dot{s})$:

$$P^* \approx c\sigma R_L(\dot{s})$$

II. For non-Newtonian fluids at zero $R_L(\dot{s})$:

$$N_1 = 2\frac{\mathrm{d}\ln P^*}{\mathrm{d}\ln \sigma} P^*$$

As to Hypothesis I, a value of $c \approx -0{\cdot}033$ is observed by others in numerical experiments.[41] Hypothesis II is known as the Higashitani–Pritchard–Baird equation.[39,41] Its derivation requires an assumption of flow symmetry about the centreline of the slot. We will show that for the Newtonian and Curtiss–Bird models employing the NRC element as we have proposed, we obtain a value of c close to the accepted value. We will show that if Hypothesis II is carefully interpreted, our results are in good agreement with its prediction in the range $0 \leqslant N_1/\sigma \leqslant 0{\cdot}6$. But a systematic bias is observed in the range $0{\cdot}6 \leqslant N_1/\sigma \leqslant 1{\cdot}3$. We believe we can explain this bias in terms of the fluid model, and thus suggest that it does not lead to any adverse inferences concerning the numerical methods employed. Before addressing the comparison of our results with Hypotheses I and II, however, we briefly dispose of issues which might be expected to affect the comparison.

7.2. *Some technical preliminaries*

7.2.1. *The corner singularity.* Following Reference 40, it is possible to estimate the order of the singularity at the corners of the mouth of the slot. The result applies to Newtonian fluids with inertial terms in a sufficiently small neighbourhood of the corner. Using the analysis of Reference 40, we deduce that for any $\varepsilon > 0$

$$\mathbf{u}^* \in [H^{1\cdot5445-\varepsilon}(\Omega)]^2$$
$$p^* \in H^{0\cdot5445-\varepsilon}(\Omega)$$

where $H^s(\Omega) = W^{s,2}(\Omega)$. Thus the singularity is very slightly weaker than that induced by an elastic plane crack (360° corner). We use no special treatment of the singularity, and therefore may expect to lose nearly half a power of h.[43] In the non-Newtonian case, the nature of the singularity is less clear, though there are some fluids which exhibit the same order singularity given above.[44] Unlike the stream-function/vorticity finite difference methods,[42,44] the finite element method allows the singularity to be entirely ignored, and that is the course we have followed in the results presented here.

7.2.2. *Results with pressure smoothing.* As is described in Reference 5, all solutions to the hole-pressure problem produce pressure fields with oscillatory pressures when the NRC is employed as described above. A typical mesh of square elements is illustrated in Figure 7, with the alternating light and dark squares indicating a chequerboard-like pattern of high and low pressures from macro to macro. Since the computed pressures are penalty approximations to p_w^h, this cannot be a matter of superposition of components of U^h on p_w^h.[31] We suspect that this pattern is a manifestation of the fact k_h tends to zero as the mesh is refined. Unlike the test problems with smoother data, the pressure smoothing has a dramatic effect in restoring a smooth pressure

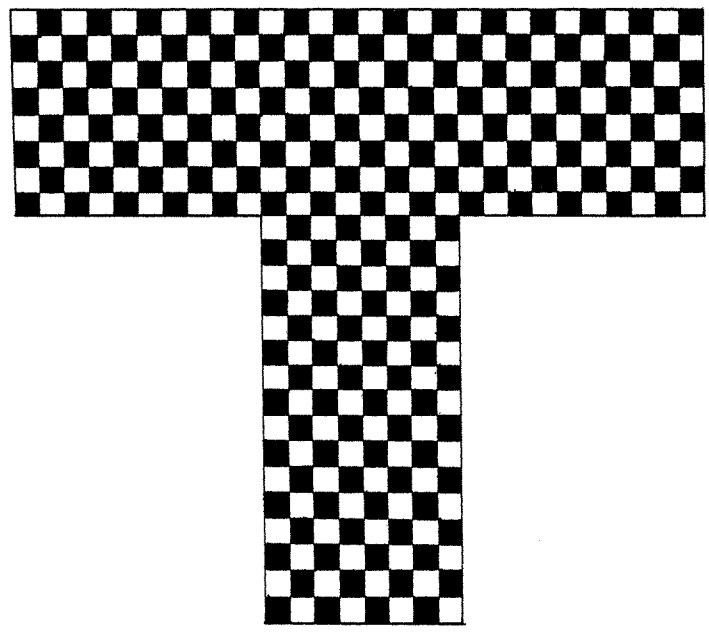

Figure 7. Regular mesh of 352 NRC macros for the hole pressure problem. Alternating white and black squares indicate observed pattern of high and low pressures in macro-averaged raw pressures

distribution, with the expected linear variation of pressure in the far ends of the channel, away from the disturbance. It is demonstrated in Reference 5 that the pressure smoothing allows an accurate determination of a reasonable value of c in Hypothesis I above, where it would be impossible to do so using the raw p_w^h. All of the results presented below employ pressures smoothed by the method described in Section 6.2.1.

7.2.3. *Computation of wall shear-stress: spatial reference points.* It is common experimental practice to measure σ, the wall shear-stress, by a physical measurement of the pressure gradient, k.[41] This can be accomplished by placing pressure transducers on wall in undisturbed flow separated by a distance L. We then have

$$k = \frac{\Delta p}{L}$$
$$\sigma = ka \tag{44}$$

where $2a$ is the width of the channel. This is a direct consequence of the equations of motion for plane Poiseuille flow. If the transducers are placed on opposite sides of the slot at a distance of $L/2$ from the centre line of the slot, it follows that the effect of the increased pressure drop due to the disturbance over the slot is $O(L^{-1})$.

Attempting to compute σ by computing $\Delta p/L$ in the finite element model produces an apparent anomaly. We consider plane Poiseuille flow without a slot. For a regular rectangular grid of NRC elements, we can argue that computation of σ via equation (44) will produce the *exact* wall shear stress of a Newtonian fluid with a given centreline velocity. But the finite element solution will produce a wall shear-stress, σ_h, in the element closest to the wall with $\sigma_h < \sigma$. The value of σ_h can be interpreted as a central difference approximation to σ at the middle of the elements closest to the wall. The difference between σ_h and σ can be significant for cruder meshes, as shown in Table I. In the present study, σ_h, the finite element wall shear-stress in undisturbed flow, was taken to be the value given in the macro on the inflow boundary, at the wall opposite the slot. One may also deduce that in plane Poiseuille flow, the smoothed pressure, $\tilde{p}^h$, at the wall nodes is most accurate when referred to the element midline, because it also is a central difference approximation at the midline.[20] We will also consider a wall shear-stress, σ_h^0, obtained by averaging the wall shear-stress in the macros at the wall, straddling the centreline of the hole. This σ_h^0 is referred to the intersection of the midline of these elements with the centreline of the hole. Thus, for reasons inherent in our methods, all computed quantities P^*, σ_h, and σ_h^0 are referred to a line half an element width in from the wall, but σ is referred to the wall.

Table I. Estimates of the constant c of Hypothesis I, using σ, σ_h, and σ_h^0. The first three cases computed with the NRC element; (*) computed by FIDAP[45] using 124 biquadratic elements and pure linear pressures; (**) computed by FIDAP using 124 biquadratic elements with four-point reduced/selective integration.[14] *Note*: For both FIDAP elements the wall shear-stress is *exactly* σ

$2a/b$	R_L	$c = P^*/Re\sigma$	$c = P^*/Re\sigma_h$	$c = P^*/Re\sigma_h^0$
1·0	1·0	−0·033	−0·038	−0·044
2·0	0·10	−0·027	−0·031	−0·031
2·0	1·00	−0·028	−0·031	−0·031
2·0*	1·00	−0·034	−0·034	—
2·0**	1·00	−0·033	−0·033	—

7.3. *Newtonian pressure differences*

For most of our computations we have used the mesh of 352 square NRC elements pictured in Figure 7. The width of the channel is $2a = 1$, the width of the hole is $b = 1$, and the depth of the hole is $d = 2$. Fully developed plane Poiseuille flow is assumed upstream and downstream from the boundaries of the domain pictured in Figure 7. To measure k in equation (44), pressures are taken at nodes at the bottom of the channel, one row of nodes in from the inflow and outflow. These nodes are separated by $L = 3{\cdot}25$. We have only eight elements across the stream, and so typically we have $(\sigma - \sigma_h) \approx 0{\cdot}125$. Note that this is exactly the mesh spacing, and thus this amount of error in σ_h is just what can be expected for errors in stresses using linear elements. We cite some computations with a mesh which has a smaller slot and more rows of elements (16 vs. 10) outside the hole. There are still eight elements in the slot and across the stream. The dimensions are $2a = 1$, $b = 0{\cdot}5$, $d = 2$ and $L = 4{\cdot}275$. Elements in the slot are half the width of elements outside the slot.

To simulate the effect of a transducer, the pressure difference P^* was computed by averaging the three values of pressure given at the three wall nodes opposite the hole, centred on the hole (nearest P_1). The weighting 1/4, 1/2, 1/4 was used. It was found that the value thus obtained did not differ substantially from the point value of the pressure at the node on the centreline, for the low Reynolds numbers considered in this subsection. Near P_2, the pressure was found to be so nearly constant that no averaging was employed.

Our major finding in this subsection is that $\sigma_h^0 < \sigma_h$ to an extent which can significantly bias the determination of the constant $c = P^*/R_L\sigma_h$ in Hypothesis I when $2a/b$ is as small as 1. This is due to the effect of the disturbance at the opposing wall in the channel flow, induced by the hole. Making $2a/b = 2$ makes the difference between σ_h^0 and σ_h negligible by removing the source of the disturbance far enough from the opposing wall. Our results are summarized in Table I. The results of Table I also show that to produce an accurate value of c, care needs to be taken to use values of P^* and σ_h, which for the technical reasons given above, are referred to the same spatial location. The difference between σ_h^0 and σ_h does not appear to be technical, but rather strongly suggests that there is a significant difference between wall shear-stress over the hole and wall shear-stress in fully developed flow in real fluids. We believe that $c = -0{\cdot}031$ is our best value for the constant of Hypothesis I and is in good agreement with the value of $c \approx -0{\cdot}033$ obtained by others.[41]

7.4. *Non-Newtonian fluids*

Our computations were carried out using the constitutive equation (3) with $T_d = 1{\cdot}82378$, $\varepsilon = 0{\cdot}08$ and $\mu_0 = 1$. As a measure of the non-Newtonian non-linearity we consider three non-dimensional numbers which are commonly used, $De = \dot{s}T_d$, $Lo = N_1/\sigma$ and $We = T_dU/2a$, where $\dot{s}$ is wall shear-rate, σ wall shear-stress, N_1 wall first normal-stress difference, U average velocity across the channel of width $2a$. All values are taken in undisturbed Poiseuille flow. As $\dot{s} \mapsto 0$, the first two numbers are asymptotically equal. We is asymptotically 1/6 the value of De. In typical computations these numbers are close in value and at the highest shear-rates $De > Lo > 6We$. Our computations fall in the range:

$$0 \leqslant De \leqslant 2{\cdot}60$$
$$0 \leqslant Lo \leqslant 2{\cdot}40$$
$$0 \leqslant 6We \leqslant 2{\cdot}28$$

We base these numbers on σ_h, $\dot{s}_h$ (the corresponding f.e.m. wall shear-rate) and N_{1h}, the f.e.m. first normal-stress difference—all taken in undisturbed flow. It will be useful to consider corresponding quantities σ_h^0, $\dot{s}_h^0$, and N_{1h}^0 taken at the centreline of the slot.

We picture our computations as applying to two different fluids with density $\rho = 1$.

Fluid F_1: polymer melt

$$T_d = 1{\cdot}82378$$
$$\varepsilon = 0{\cdot}08$$
$$\mu_0 = 10^4$$
$$\text{In the range } 0 \leqslant \dot{s} \leqslant 0{\cdot}93$$

Fluid F_2: polymer solution

$$T_d = 0{\cdot}45$$
$$\varepsilon = 0{\cdot}08$$
$$\mu_0 = 1$$
$$\text{In the range } 0 \leqslant \dot{s} \leqslant 5{\cdot}78$$

The parameters were not actually varied in the computations, but amount to two interpretations of the same $\dot{s}T_d$. For F_1 in the attainable range of solutions, Re and $R_L(\dot{s})$ are negligible, so we picture our results at zero Reynolds number, which test Hypothesis II, as begin flows of fluid F_1. In this case stresses should be scaled up by a factor of 10^4.

To obtain qualitative comparisons with the pictures of flows of polymer solutions in Reference 38, and to make physical sense of Reynolds numbers of the order of 1 to 32, fluid F_2 is a more appropriate interpretation. Computed stresses are scaled correctly for fluid F_2, but the computed strain-rates should be scaled up by a factor of about 4·05. We are well aware that Curtiss and Bird intended their model to apply to *undiluted* polymers, and fluid F_2 may be unrealistic. Comparison with the fluids modelled and observed in Reference 38 suggests that our fluid F_2 shear-thins much more drastically than actual polymer solutions. This may be artificial, but interesting nevertheless, becasue it magnifies inertial effects at fixed De.

7.4.1. *Non-Newtonian pressure differences.* A careful interpretation of Reference 39 shows that Hypothesis II should be viewed as applying to P^*, N_{1h}^0, and σ_h^0, that is to quantities measured on the centreline of the slot. Our studies in this regard were performed for creeping flow in which computationally $\rho \equiv 0$. We took flows of fluid F_1 with various centreline velocities specified to produce the elastic part of the pressure difference, P_e, is the whole of P^*.

It is convenient to consider the integral form of Hypothesis II:

$$P_e = \frac{1}{2}\int_0^{\sigma} \frac{N_1}{\tau}\, d\tau \tag{45}$$

Implicit in the assumptions required to make Hypothesis II valid is that equation (45) can be evaluated using N_1 and τ taken at the wall opposing the slot in a sequence of experiments and that the result will be the same as if the values had been taken in a single experiment between a point at which $\tau = 0$ and the wall,[7] where $\tau = \sigma$. For the reasons given above, in our numerical tests the value for σ used in equation (45) is actually σ_h^0.

In Figures 8 and 9, we summarize a test of Hypothesis II. We plotted N_{1h}^0/σ_h^0 as a function of σ_h^0 for all of our computations with fluid F_1, using a channel with $2a/b = 1$, 1·5 and 2 (obtained by changing $2a$ appropriately on our 352 element mesh). These data produced a master curve of N_{1h}^0/σ_h^0 with all points appearing to fall on the same curve in Figure 8. Integrating under the curve of Figure 8 by the composite trapezoidal rule gives the curve in Figure 9, which predicts P_e based

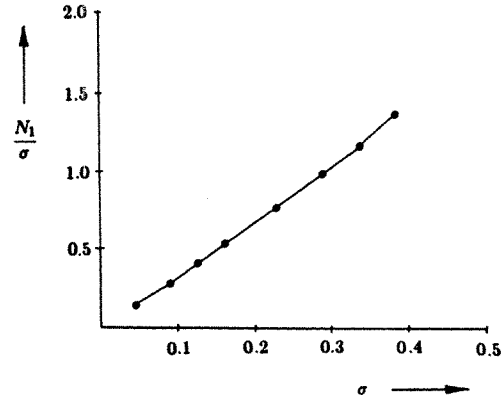

Figure 8. N^0_{1h}/σ^0_h (measured over slot) as a function of σ^0_h in flows over slot with undisturbed flows at $De \leqslant 1{\cdot}7$

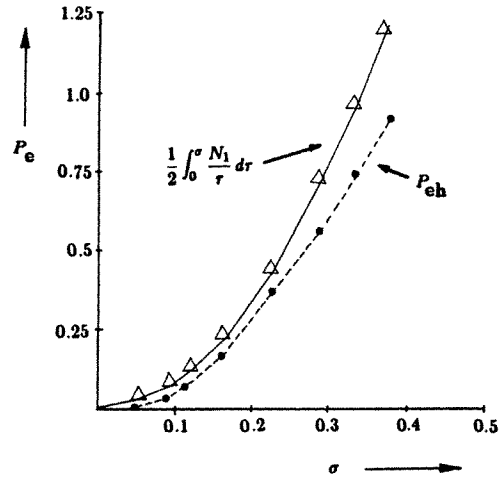

Figure 9. The HPB prediction (solid curve) versus actual calculated pressure differences over the slot, P_{eh} (dotted curve). Prediction is based on the data of Figure 8; P_{eh} is computed directly from the f.e.m. stresses

on N^0_{1h} and the interpretation of equation (45) in which the integrand can be taken from wall values of the relevant quantities in a sequence of experiments. We note that the actual values of P_e taken from the f.e.m. model are in good agreement with the prediction of Hypothesis II, only in the range $0 \leqslant N^0_{1h}/\sigma^0_h \leqslant 0{\cdot}6 (0 \leqslant \sigma^0_h \leqslant 0{\cdot}18 \times 10^4)$. In the rest of the range $0{\cdot}6 \leqslant N^0_{1h}/\sigma^0_h \leqslant 1{\cdot}28$, the agreement deteriorates to about a 20 per cent deviation of the f.e.m. prediction from the prediction of Hypothesis II. Since we have earlier observed about a 12·5 per cent error in stresses, and since the prediction of Hypothesis I was met with such accuracy, we tend to believe that the 20 per cent error here is physically significant.

We believe that there is an explanation for this lack of agreement based on the fluid model, not the numerical model. Figure 10 plots two streamlines, the separating streamline and a nearby vortex streamline at $N^0_{1h}/\sigma^0_h = 1{\cdot}28$. There is clearly visible asymmetry of a nature characteristic of flows of elastic fluids.[38] This is in violation of the assumptions underlying Hypothesis II. This asymmetry perhaps could explain the deviation at $N^0_{1h}/\sigma^0_h = 1{\cdot}28$, but it evidently does not explain the deviation of about 23 per cent from the prediction of Hypothesis II observed at $N^0_{1h}/\sigma^0_h = 0{\cdot}73$.

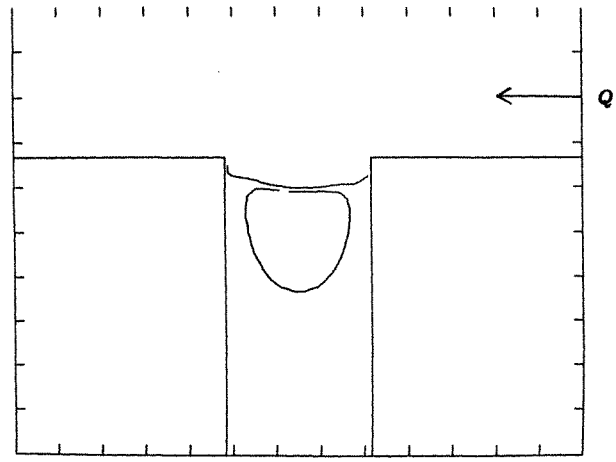

Figure 10. Flow from right to left over a transverse slot with $De = 1{\cdot}03$ and $Re = 0$. Shown are separating streamline and nearby streamline in the vortex

Inspection of the results shows much less asymmetry in that case, but, if anything, a poorer agreement with Hypothesis II. Rather, we propose that a necessary supposition for Hypothesis II to hold is that the function N_1/σ, measured at the wall in a *sequence* of experiments must be the same function of σ as N_1/τ is of τ, in any *single* experiment. In the latter case $\tau = \tau(x)$ varies from $\tau(0) = 0$ at the channel centreline to $\tau(a) = \sigma$, at the wall. But direct inspection of the numerical results shows that this is not the case, with the difference between the two functions becoming pronounced at $N_{1h}^0/\sigma_h^0 = 0{\cdot}73$. This happens even with quite symmetrical streamline, because N_{1h}^0/σ_h^0 is measured in a shearing flow with a shearing history. N_1/τ on the centreline may be taken in a shearing flow, but because of the disturbance induced by the hole, the *history* is not one of simple shear. A more detailed study of this may be found in References 8 and 46.

We believe that we have identified two possible sources of bias in Hypothesis II as applied to measurements of N_1, and both can be traced to the disturbance induced by the hole. First, N_1^0 and σ^0 must be compared, rather than the more convenient N_1 and σ, or else slots with $2a/b > 1$ must be employed; $2a/b \geqslant 2$ was found to be sufficient. Secondly, the effect of the disturbance over the hole perturbs the centreline particle histories enough to significantly violate the symmetry and shearing history assumptions behind Hypothesis II when long-range memory of the fluid is significant.

These results are at odds with the results reported in Reference 41 for pressure differences over circular holes. Perhaps these holes produce a relatively smaller disturbance than a slot. Using holes may be a viable alternative to slots if future laboratory experiments bear out our numerical experiments. But using holes still may not cure the bias, because the differential form of Hypothesis II seems to require for its derivation that N_1/τ be the same function of τ between each pair of maxima and minima of τ along the centreline from the channel wall to the hole bottom.[8,46] This may be significantly violated because of differing particle histories along the centreline—even with holes. The best alternative may be to carefully co-ordinate numerical and laboratory experiment and compute a calibration curve which corrects for both sources of bias identified above.

7.4.2. *Qualitative observations on elasticity and inertia.* One of the interesting conclusions of the experimental and numerical studies in Reference 38 is that, in some ways, the effects of inertia and elasticity oppose each other in flows over transverse slots. In the following discussion we refer to flow-visualizations from Reference 38 but do not reproduce those photographs here. In Figure 10 we see that the separating streamline in non-Newtonian flow has been deformed so that a line

normal to it tills upstream, and correspondingly, the vortex is distended with its highest point on the downstream side. For inertially dominated flows the effect is quite the opposite, as illustrated for the Newtonian flow at $Re = 20{\cdot}0$ of Figure 11. Those observations are in qualitative agreement with the results of Reference 38. The numerical results computed with finite differences presented in Reference 38.

At high De, there are similarities and differences between our results and those of Reference 38. Figure 12 shows the separating streamline and a streamline on the vortex for fluid F_2 at $6We = 2{\cdot}28$, $Re = 3{\cdot}0$. We find here a combined effect of elasticity and inertia. As appears to be characteristic of flows of elastic fluids over slots,[38] the separating streamline is depressed further into the hole than in for a Newtonian fluid. Figure 12 involves a channel with $2a/b = 0{\cdot}5$, which is the case in Reference 38. Our Newtonian, $Re = 0{\cdot}0$ results show that the deepest penetration of the separating streamline into the slot is $0{\cdot}4b$. But in the non-Newtonian case of Figure 12, the deepest penetration is $0{\cdot}5b$. In Reference 38, numerical results are presented for $Re = 3{\cdot}0$ and $6{\cdot}0$ at this same We. The numerical results of Reference 38 show the deepest penetration to be about $0{\cdot}5b$ for

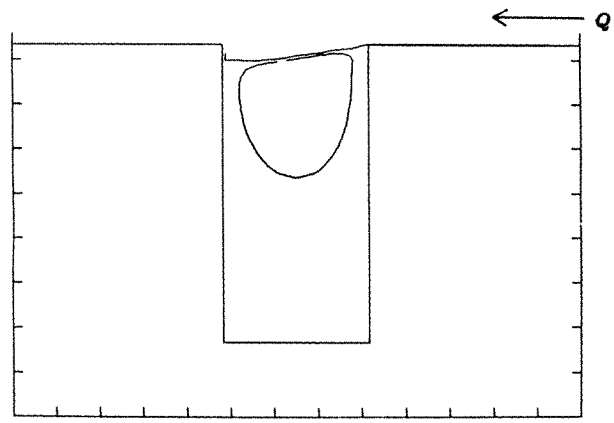

Figure 11. Flow over a transverse slot similar to Figure 10, but with $De = 0$ and $Re = 20{\cdot}0$

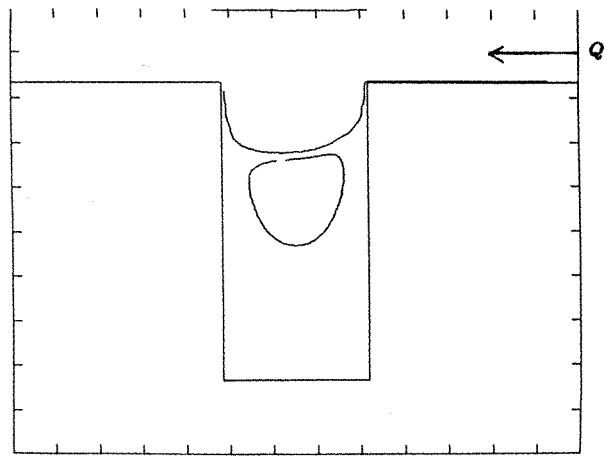

Figure 12. Flow over a transverse slot similar to Figure 10, but with $De = 2{\cdot}60$, $Re = 3{\cdot}0$, and $R_L = 31{\cdot}7$

both values of Re. The experimental results seem to put the deepest penetration between 0·5 and 0·6b, at $Re = 3{\cdot}0$, but it is hard to measure the photograph with precision.

The numerical results given in Reference 38 are with an Oldroyd fluid model. The authors do not give $\dot{s}$ for their computations, but in our computations at this De, we find that $\dot{s} = 6{\cdot}834U/2a$. From the given values of other parameters and We in Reference 38, we estimate that $\dot{s}$ is no larger than 7 in their calculations. If this estimate is anywhere near correct, we can see that the Oldroyd fluid has thinned only a small amount compared to our Curtiss–Bird model, which has thinned to less than a third of its zero-shear viscosity at the wall in undisturbed flow. We believe that what we are seeing in Figure 12 is a streamline *depression* into the slot which is characteristic of non-Newtonian flows and a streamline *tilt* characteristic of inertially dominated flows. If our estimates of $\dot{s}$ for the flows of Reference 38 do not grossly underestimate $\dot{s}$, the value of $R_L(\dot{s})$ are lower there than the value $R_L(\dot{s}) = 31{\cdot}7$ that we calculate for Figure 12. This, we believe, explains why the streamlines of the numerical model in Reference 38 show little if any tilt, whereas ours definitely tilt towards the 'inertial side'. We speculate that the reason the experimental vortex in Reference 38 shows a tilt towards the elastic side is that the experimental fluid has thinned even less than either numerical model.

It is interesting to note that, along with the inertial tilt of the vortex in Figure 12, P^* is negative. We can be confident that if this flow had $Re = 0$, we would have $P^* \equiv P_e > 0$, and that the vortex would be on the 'elastic side' of the slot. Our results combined with Reference 38 strongly suggest that as $R_L(\dot{s})$ varies at fixed We, the depression of the separating streamline into the slot remains relatively fixed, but the vortex moves from elastic to inertial side with attendant change in the sign of P^*. Thus we see that elastic and inertial effects do not oppose each other in the sense of rendering the resultant flow apparently Newtonian, but superpose to make a flow which has indentifiable characteristics of each source of non-linearity.

8. CONCLUSIONS

We believe that the NRC crossed triangle element is an ideal element for steady flows of memory fluids. The rigorous analysis of numerical methods for non-Newtonian flows is in its infancy, and the error analysis of finite elements which fail the discrete LBB condition in Newtonian flows does not provide as complete picture as could be desired. Nevertheless, we believe that the theoretical results for linear problems given here provide a logical scenario, explaining why such elements can give convergent approximations when employed with care. Even though we have not proved that the NRC element requires only two L_2 derivatives of the exact solution to obtain an optimal convergence rate, we believe, based on our numerical experiments, that the result is true.

The advantages provided by exact incompressibility of Lagrange multiplier f.e.m. solutions, and the attendant existence of stream and drift functions have been shown to be of fundamental importance to implementation of our numerical procedures for memory fluids. The fact that the NRC has constant gradients on each triangle has been shown to be vital in the analytic determination of particle paths and transit times. The several advantages just mentioned make the NRC element completely unique among finite elements for plane and axisymmetric incompressible flows. We believe that this uniqueness is ample justification for putting up with the added computational cost of the internal macro node. The internal node has been shown to provide dependent degrees of freedom which aid in the attaining of exact incompressibility. When these degrees of freedom are constrained by nearby boundaries, we have seen that the result is a simple shearing flow appropriate to a viscous boundary layer.

Because there are some theoretical questions unanswered, we have dwelled at some length on numerical results. At low Reynolds numbers, we have found that surprising agreement with

accepted results[41] for P^* measurements can be obtained with 350 to 450 macros—this in spite of the fact that we use no special treatment of the corner singularities which have caused concern for finite difference practitioners.[38,42,44] We have seen that pressure solutions using the NRC element can indeed be severely affected by 'generalized' chequerboard phenomena.[5,29] The numerical results presented here suggest that the proposed pressure-smoothing method cures this apparent pathology and is easy to implement.

At higher Reynolds number and at any non-zero *De*, there is little in the way of error analysis to fall back on. We have seen that at $Re = 20{\cdot}0$, the numerical results show significant inertial effects and that there is good qualitative agreement between our results and published numerical and experimental results.[38] For non-Newtonian fluids, our results with the Curtiss–Bird model agree well with published experimental and numerical results[38,41] in the second-order fluid range. At higher *De*, our results have been seen to compare well qualitatively to pictures of non-Newtonian flows when the Reynolds number is low.[38] We believe that the discrepancies we have observed using the Curtiss–Bird model in regard to vortex placement and predictions of P_e based on N_1 are genuine consequences of the fluid model. In the former case, we believe that we have identified an interesting interaction between shear-thinning, elasticity and inertia. In the latter case, we believe that our studies have identified important consequences to hole-pressure measurements involving the interaction of long-range memory effects and the disturbance induced by the slot. We have argued, in each case where our results are at odds with preconception, that the discrepancy is part of a coherent physical picture painted by our numerical model. We offer these numerical results, agreements and discrepancies, with the confidence that they will stand ultimately as the firmest evidence of the usefulness of the NRC element.

ACKNOWLEDGEMENT

The research described here was done while the authors were at Illinois Institute of Technology. The research on the development of numerical methods for non-Newtonian fluid flow was sponsored by N. S. F. Grants MCS-79-03542, MCS-81-02089, and MCS-83-01433. The research on error estimates for finite elements for incompressible media was sponsored by N. S. F. Grant CME-80-17549. The final revised manuscript was prepared at the Mathematics Research Center, University of Wisconsin—Madison, where the second author is sponsored by the United States Army under Contract No. DAAG29-80-C-0041.

REFERENCES

1. B. Bernstein, M. K. Kadivar and D. S. Malkus, 'Steady flows of memory fluids with finite elements: two test problems', *Comp. Meths. Appl. Mech. Eng.*, **27**, 279–302 (1981).
2. M. Viriyayuthakorn and B. Caswell, 'Finite element simulation of viscoelastic flows', *J. Non-Newtonian Fluid Mech.*, **8**, 245–267 (1981).
3. J. Nagtigaal, D. M. Parks and J. R. Rice, 'On numerically accurate finite element solutions in the fully plastic range', *Comp. Meths. Appl. Mech. Eng.*, **4**, 153–178 (1974).
4. B. Mericier, 'A conforming finite element method for two dimensional, incompressible elasticity', *Int. J. Numer. Meth. Eng.*, **14**, 942–945 (1979).
5. D. S. Malkus and E. T. Olsen, 'Obtaining error estimates for optimally constrained incompressible finite elements', *Comp. Meths. Appl. Mech. Eng.*, **45**, 331–353 (1984).
6. F. Chen and B. Bernstein, 'The artificial time drift-function method for finite element techniques for axisymmetrical flows of memory fluids', *Report for N.S.F. Grant MCS-81-02089*, Department of Mathematics, Illinois Institute of Technology, Chicago, 1982.
7. J. H. Argyris, J. St. Doltsinis, W. C. Knudson, J. Szimmat, H. Wüstenberg and K. Willam, 'Eulerian and Lagrangian techniques for elastic and inelastic large deformation processes', *I.S.D. Report No. 256* 1976.
8. D. S. Malkus and B. Bernstein, 'Flow of a Curtiss–Bird fluid over a transverse slot using the finite element drift-function method', *J. Non-Newtonian Fluid Mech.*, in press.

9. C. Curtiss and R. B. Bird, 'Kinetic theory for polymer melts. Parts I and II, *J. Chem. Phys.* **74,** 2016–2033 (1981).
10. P. K. Currie, 'Constitutive equations for polymer melts predicted by the Doi–Edwards and Curtiss–Bird kinetic theory models', *J. Non-Newtonian Fluid Mech.*, **11,** 53–68 (1982).
11. C. J. S. Petrie, 'Measures of deformation and convected derivatives', *J. Non-Newtonian Fluid Mech.*, **5,** 147–176 (1975).
12. M. Doi and S. F. Edwards, 'Dynamics of concentrated polymer systems. Parts I–IV, *J.C.S. Faraday*, **74** and **75,** 1789–1801 (1978), 1802–1817 (1978), 1818–1813 (1978), 38–54 (1979).
13. G. Golub, 'Some modified matrix eigenvalue problems', *SIAM Review*, **15,** 318–334 (1973).
14. B. Bernstein and D. S. Malkus, 'Steady flows of memory fluids. A progress report', *Report for N.S.F. Grant MCS-81-02089*, Department of Mathematics, Illinois Institute of Technology, Chicago, 1981.
15. D. S. Malkus and T. J. R. Hughes, 'Mixed finite element methods—reduced and selective integration techniques: a unification of concepts', *Comp. Meths. Appl. Mech. Eng.*, **15,** 63–81 (1978).
16. D. S. Malkus, 'Penalty methods in finite element analysis of fluids and structures', *Nuc. Eng. Design.*, **57,** 441–448 (1980).
17. J. N. Reddy, 'On penalty function methods in finite element analysis of flow problems', *Int. J. Numer. Methods Fluids*, **2,** 151–171 (1982).
18. A. Ralston and P. Rabinowitz, *A First Course in Numerical Analysis*, McGraw-Hill, New York, 1978.
19. D. S. Malkus, 'Functional derivatives and finite elements for the steady spinning of a viscoelastic filament', *J. Non-Newtonian Fluid Mech.*, **8,** 223–237 (1981).
20. T. J. R. Hughes, W. K. Liu and A. Brooks, 'Finite element analysis of incompressible viscous flows by the penalty function formulation', *J. Comp. Phys.*, **30,** 1–60 (1979).
21. H. H. Winter, 'Modelling of strain histories for memory fluids in steady axisymmetric flows', *J. Non-Newtonian Fluid Mech.*, **10,** 157–167 (1982).
22. H. Court, K. Walters and R. Davies, 'Long-range memory effects in flows involving abrupt changes in geometry. Part 4: numerical simulation using integral rheological models', *J. Non-Newtonian Fluid Mech.*, **8,** 95 (1981).
23. P. Ciarlet, *The Finite Element Method for Elliptic Problems*, North-Holland, Amsterdam, 1978.
24. K. J. Bathe and E. L. Wilson, *Numerical Methods in Finite Element Analysis*, Prentice-Hall, Englewood Cliffs, 1976.
25. F. Brezzi, 'On the existence, uniqueness and approximation of saddle point problems arising from Lagrangian multipliers', *R.A.I.R.O. Analyse Numerique*, **8,** 129–151 (1974).
26. M. Fortin, 'Old and new elements for incompressible flows', *Int. J. Numer. Methods Fluids*, **1,** 347–364 (1981).
27. C. Johnson and J. Pitkäranta, 'Analysis of some mixed finite element methods related to reduced integration', *Math. Comp.*, **38,** 375–400 (1982).
28. J. T. Oden, N. Kikuchi and Y. J. Song, 'Penalty finite element methods for Stokesian flows', *Comp. Meths. Appl. Mech. Eng.*, **31,** 297–329 (1982).
29. R. L. Sani, P. M. Gresho, R. L. Lee, D. F. Griffiths and M. Engelman, 'The cause and cure (?) spurious pressures generated by certain FEM solutions to the incompressible Navier–Stokes equations. Part I and II, *Int. J. Numer. Methods Fluids*, **1,** 17–43 (Part I), 171–204 (Part II) (1981).
30. M. Fortin, 'An analysis of convergence of mixed finite element methods', *R.A.I.R.O. Analyse Numerique*, **8,** 341–354 (1977).
31. D. S. Malkus, 'Eigenproblems associated with the discrete LBB condition for incompressible finite elements', *Int. J. Eng. Sci.*, **19,** 1299–1310 (1981).
32. E. T. Olsen, 'Stable finite elements for non-Newtonian flows; first order elements which fail the LBB condition', *Ph.D. Thesis*, Department of Mathematics, Illinois Institute of Technology, Chicago, 1983.
33. I. Babuska and A. K. Aziz, *Mathematical Foundations of the Finite Element Method*, Academic Press, New York, 1972.
34. B. Mercier, *Topics on Finite Element Solution of Elliptic Problems*, Tata Institute of Fundamental Research in Bombay Lecture Series, Springer-Verlag, Berlin, 1979.
35. I. Fried and D. S. Malkus, 'Mass matrix lumping by numerical integration with no convergence rate loss', *Int. J. Solids Structures*, **11,** 461–466 (1975).
36. A. Thom and C. J. Apelt, *Aeronaut. Res. Council Tech. Report R. and M. No. 3090*, London, 1958.
37. N. R. Jackson and B. Finlayson, 'Calculation of hole pressure: I. Newtonian fluids, II. Viscoelastic fluids', *J. Non-Newtonian Fluid Mech.*, **10,** 55–69 (1982).
38. T. Cochrane, K. Walters and M. F. Webster, 'On Newtonian and non-Newtonian flow in complex geometries', *Phil. Trans. Roy. Soc. London*, **301,** 163–181 (1981).
39. K. Higashitani and W. G. Pritchard, 'A kinematic calculation of intrinsic errors in pressure measurements made with holes', *Trans. Soc. Rheology*, **16,** 687–696 (1972).
40. H. Moffat, 'Viscous and restive eddies near a sharp corner', *J. Fluid Mech.*, **18,** 1–18 (1963).
41. A. S. Lodge and L. de Vargas, 'Positive hole-pressures and negative exit pressure generated by molten low-density polyethylene flowing through a slit die', *Rheologica Acta*, **22,** 151 (1983).
42. H. Holstein, Jr. and D. J. Paddon, 'A singular finite difference treatment of re-entrant corner flow. Part I: Newtonian fluids', *J. Non-Newtonian Fluid Mech.*, **8,** 81–93 (1981).
43. J. O'Leary, *Ph.D. Thesis*, University of Texas, Austin, 1981.
44. H. Holstein, Jr., 'A singular finite difference treatment of re-entrant corner flow. Part II: Oldroyd fluids', preprint.
45. M. S. Engelman, 'FIDAP—A fluid dynamics analysis package', *Adv. Software Eng.*, **4,** 163 (1982).
46. Marie Y.-B. Ju, *M.S. Thesis*, Illinois Institute of Technology, Chicago, 1984.
47. M. J. Lighthill, 'Drift', *J. Fluid Mech.*, **1,** 31–53 (1956).